



Nickel-doped tungsten oxide promotes stable and efficient hydrogen evolution in seawater

Wanli Liang^{a,b}, Mengyan Zhou^a, Xinyi Lin^a, Jinchang Xu^a, Pengyu Dong^a, Zhichen Le^a, Muzi Yang^c, Jian Chen^c, Fangyan Xie^c, Nan Wang^a, Yanshuo Jin^{a,*}, Hui Meng^a

^a Siyuan Laboratory, Guangzhou Key Laboratory of Vacuum Coating Technologies and New Energy Materials, Guangdong Provincial Engineering Technology Research Center of Vacuum Coating Technologies and New Energy Materials, Guangdong Provincial Key Laboratory of Optical Fiber Sensing and Communications, Department of Physics, Jinan University, Guangzhou, Guangdong 510632, PR China

^b School of Chemistry and Chemical Engineering, South China University of Technology, Guangzhou, Guangdong 510641, PR China

^c Instrumental Analysis & Research Center, Sun Yat-Sen University, Guangzhou, Guangdong 510275, PR China

ARTICLE INFO

Keywords:

Hydrogen evolution
Seawater
Tungsten oxide
Doping
Non-precious metal

ABSTRACT

Hydrogen is considered as an efficient energy alternative, and the use of offshore wind power to electrolyze seawater to produce hydrogen will become the future model. Here, nickel-doped tungsten oxide is proposed to realize hydrogen production from seawater. Ni-WO_x@NF was prepared experimentally, in which Ni was doped into WO_x to replace part of the W sites. There is a volcanic relationship between the amount of Ni doping and the activity of the hydrogen evolution reaction. Particularly in alkaline seawater, Ni-WO_x@NF only needs an overpotential of 45.69 mV to reach a current density of 10 mA cm⁻² and exhibits stability over 120 h. In addition, theoretical calculations confirmed that Ni doping can optimize the activity of hydrogen evolution reaction. This work proposes that nickel doping can enhance the hydrogen evolution reaction activity of tungsten oxide with excellent corrosion resistance, enabling it to work efficiently and stably in alkaline seawater.

1. Introduction

Extensive use of fossil energy in industrial production will emit a large amount of CO₂, and other greenhouse gases, leading to global warming and environmental pollution [1]. Hydrogen energy is considered to be one of the most feasible renewable energy conversion strategies, but due to the high price of precious metal catalysts and the high consumption of high purity fresh water, large-scale water electrolysis is limited to further application in catalysis. The use of offshore wind power to electrolyze seawater to produce hydrogen will become the future model. Seawater has a huge content on the earth, accounting for about 97 % of the water resources, and the existence of various cations can improve electrical conductivity [1,2]. In recent years, hydrogen production by electrolysis of seawater has been widely confirmed. However, when noble metals are used as hydrogen evolution reaction (HER) electrocatalysts, the highly corrosive hypochlorite by-products generated at the reaction electrode can block the active sites of the noble metal catalysts [3,4]. To adapt to larger-scale applications, it is necessary to develop highly efficient and stable electrocatalysts for seawater splitting containing only non-precious metals.

Recently, various alkaline freshwater/seawater electrocatalysts have been extensively reported, with both activity and cost advantages [5]. Xu et al. proposed that carbon-doped porous cobalt phosphide (C-Co₂P) prepared by electrochemical dealloying can achieve high-efficiency seawater splitting for hydrogen production. Replacing P with C can adjust the electronic structure and reduce the d-band center of Co, thereby lowering the water adsorption and dissociation energies [3]. Heteroatom doping is considered to be one of the effective strategies to enhance HER activity, as it leads to charge redistribution and electronic structure modulation to optimize the water dissociation energy and hydrogen/hydroxide adsorption free energy [1]. To meet the needs of industrial production, the design of the catalyst should not only improve the activity but also have a high specific surface area and good stability. Although there are many reports on hydrogen evolution from alkaline seawater, it is necessary to further improve the activity and corrosion resistance of the catalyst and develop a simpler method [6].

Tungsten oxide is considered as one of the most attractive electrocatalysis due to its environment-friendly, chemically stable, adjustable composition and structure [7]. However, tungsten oxide has poor conductivity and limited active sites, so it is necessary to improve HER

* Corresponding author.

E-mail addresses: jinyanshuo@email.jnu.edu.cn, jinyanshuo@qq.com (Y. Jin).

<https://doi.org/10.1016/j.apcatb.2023.122397>

Received 26 August 2022; Received in revised form 20 December 2022; Accepted 10 January 2023

Available online 11 January 2023

0926-3373/© 2023 Elsevier B.V. All rights reserved.

activity by changing the geometric and electronic structures [8,9]. Nickel foam (NF) is widely used as catalyst carrier due to its high porosity, which provides more space for catalyst growth and maximizes electrolyte contact [10]. Nickel foam also acts as a nickel source in some works, such as Ni₂P/NF [11], Ni-W₂N/NF [12], S-(Ni,Fe)OOH [13], MoS₂(1-x)Se_{2x}/NiSe₂ [14]. Shen's group proposed a simple synthesis method, in which nickel foam can be used as both a substrate and a reducing agent, and the resultant porous MoO₂ can provide high surface area and multiple active sites [15]. Thus, the use of nickel foam is expected to provide a simple way to regulate tungsten oxide and achieve high efficiency hydrogen evolution in alkaline seawater.

In this work, we synthesized nickel-doped tungsten oxide nanorods (Ni-WO_x) using a simple two-step method for efficient hydrogen evolution in alkaline freshwater/seawater. Ni doping can effectively enhance the HER activity of WO_x. As a result, Ni-WO_x@NF requires only small overpotentials of 40.51 and 137.04 mV to reach current densities of 10 and 100 mA cm⁻² and has excellent long-term stability. Moreover, it exhibits excellent activity in alkaline seawater, achieving an HER current density of 10 mA cm⁻² at only 45.69 mV, and exhibits stability over 120 h. Density functional theory (DFT) analysis shows that Ni doping optimized the free energy of hydrogen adsorption at the O site and the hydroxide adsorption free energy at the W site, thereby enhancing the HER activity. Our study highlights that heteroatom doping can adjust the electronic structure of oxide electrocatalysts for enhanced HER performance, providing a feasible way for hydrogen production from alkaline seawater.

2. Experimental section

2.1. Chemicals

Ammonium polytungstate [(NH₄)₆W₇O₂₄·6H₂O] was purchased from Tianjin Jinke Fine Chemical Research Institute. Tungsten powder (W) was purchased from Shanghai Aladdin Biochemical Technology Co., LTD. Nickel foam and cobalt foam (CF) were purchased from Kunshan Jiayisheng Electronics Co., LTD. Pt/C and Nafion were purchased from Shanghai Hesen Electric Co., LTD. Potassium hydroxide (KOH) and hydrochloric acid (HCl) were purchased from Guangzhou Chemical Reagent Factory. Sea salts was purchased from Sigma-Aldrich. The seawater used in this study was from Weihai.

2.2. Synthesis of Ni-WO_x@NF-pre

Firstly, a piece of nickel foam with a size of 40.0 mm × 20.0 mm × 1.0 mm was prepared and soaked in 1:1 v:v hydrochloric acid solution for about 20 min. Subsequently, 30 mL of 30 mmol/L (NH₄)₆W₇O₂₄·6H₂O was added to a 50 mL Teflon-lined autoclave, and the pretreated NF was placed vertically. The encapsulated autoclave was transferred to an oven at 150 °C for 24 h. The product was rinsed with deionized water and dried in an oven at 60 °C for about 2 h to obtain the NF-supported catalyst precursor (Ni-WO_x@NF-pre).

2.3. Synthesis of Ni-WO_x@NF

The NF with the precursor was placed on the porcelain boat and annealed in N₂ and H₂ atmosphere at 600 °C for 1 and 2 h, respectively, at a heating rate of 10 °C/min. The obtained sample is nickel-doped tungsten oxide, labeled as Ni-WO_x@NF. Compared with the pretreated NF, the loading of Ni-WO_x@NF is 37 mg cm⁻².

In the control experiment, the concentration of (NH₄)₆W₇O₂₄·6H₂O in the synthesis process was adjusted. The (NH₄)₆W₇O₂₄·6H₂O of 5, 10, 20, 30, and 50 mmol/L were compared, and the corresponding products were labeled as Ni-WO_x-5@NF, Ni-WO_x-10@NF, Ni-WO_x-20@NF, Ni-WO_x@NF, and Ni-WO_x-50@NF, respectively.

2.4. Synthesis of WO_x

First, some commercial tungsten was placed in a porcelain boat and kept in the air at 600 °C for 2 h to fully oxidize. Then, the obtained material was annealed at 600 °C for 1 and 2 h in N₂ and H₂ atmospheres, respectively, and the obtained material was WO_x.

2.5. Preparation of WO_x@NF and Pt/C@NF

To compare the electrochemical performance of the materials in the same state as the experimental group, the WO_x and commercial Pt/C were loaded on NF for electrochemical tests.

To prepare the catalyst slurry of WO_x@NF, 1.8 mg of WO_x and 9 μL of 5 % Nafion were added to 200 μL of ethanol and sonicated for 40 min to obtain a homogeneous solution. Then, the ink was dropped on a piece of NF with a size of 5.0 mm × 5.0 mm × 1.0 mm to obtain the WO_x@NF. Therefore, the loading of WO_x is 7.2 mg cm⁻².

To prepare the Pt/C@NF, the catalyst ink was prepared from 0.5 mg of 40 % commercially Pt/C, 1 μL 5 % Nafion, and 250 mL ethanol. After that, the ink was dropped onto the surface of a piece of NF with the size of 5.0 mm × 5.0 mm × 1.0 mm. Thereby, Pt/C@NF was prepared with a mass load of 2.0 mg cm⁻².

2.6. Preparation of Co-WO_x@CF and WO_x@CF

The preparation of Co-WO_x@CF and WO_x@CF is similar to that of Ni-WO_x@NF and WO_x@NF. Specifically, the NF in the synthetic process is replaced by CF of the same size.

2.7. Characterization method

Field emission scanning electron microscopy (FESEM; SU8220, HITACHI UHR) was used to observe and record the morphology of the catalysts with an accelerating voltage of 10,000 volts. X-ray diffractometer (XRD; MiniFlex 600, Rigaku) was used to determine the crystal structure of materials with a scanning speed of 5°/min. Raman spectroscopy (LabRAM HR Evolution, HORIBA Jobin Yvon S.A.S) was used to study the structure of molecules. High-resolution transmission electron microscopy (HRTEM; JEM 2100F, Rigaku) was used to analyze the structure and elemental distribution of the catalysts. X-ray photoelectron spectroscopy (XPS; K-ALPHA+, Thermo Fisher Scientific) and ultraviolet photoelectron spectra (UPS; AXIS SUPRA+, Kratos) were used to analyze the elements and valence states of materials. X-ray Absorption fine structures (XAFS) were obtained at the Singapore Synchrotron Light Source (SSLS) and Super Photon ring-8 (SPRING-8), and the data were processed by Demeter [16]. And the resistivity of the catalyst was analyzed by 4-Point Probes Resistivity Measurement System.

2.8. Electrochemical measurement

Electrochemical tests were performed in a conventional three-electrode system. The obtained catalyst was cut into small pieces with a size of 5.0 mm × 5.0 mm × 1.0 mm and placed on the working electrode. In addition, the reference electrode is a Hg/HgO electrode, and the counter electrode is a graphite rod. In this work, the potentials shown are all referenced to the reversible hydrogen electrode (RHE), which was corrected experimentally by using Pt/C as the working electrode potential in the H₂-saturated solution. The electrolytes were 1 M KOH, 1 M KOH seawater solution and 1 M KOH seasalt solution, with pH values of 13.45, 13.10, and 13.15, respectively. 1 M KOH seawater was prepared by adding 80 mmol KOH to natural seawater to form 80 mL of homogeneous solution, referring to the work of Qiao's et al. [17]. And 1 M KOH seasalt solution was prepared by dissolving 80 mmol KOH and 3.2 g of sea salts into deionized water to form a 80 mL solution. In addition, the given current densities are normalized to the geometrical area unless otherwise specified.

The HER polarization curves were measured using linear sweep voltammetry with a measurement range of 10 to -300 mV and a scanning speed of 1 mV/s. Electrochemical impedance spectroscopy (EIS) was measured at the voltage of -100 mV vs. RHE with a voltage perturbation of 10 mV over the frequency range of 200 kHz to 100 mHz. In addition, the long-term stability was measured by the chronopotentiometry technique.

2.9. Calculation method

The DFT calculations were performed using the Vienna Ab-initio Simulation Package with the frozen-core all-electron projector-augment-wave method [18–21]. The Perdew-Burke-Ernzerhof of generalized gradient approximation was used to describe the exchange and correlation potential [22]. The cutoff energy for the plane-wave basis set was set to 450 eV \AA^{-1} . 2×1 WO_2 (011) supercell with 3-layers atoms and a vacuum region of 15 \AA above them was used to ensure the decoupling between neighboring systems. For the geometry optimization, the atoms in the bottom layer of slabs were fixed to their bulk positions. The geometry optimizations were performed until the forces on each ion were reduced below 0.01 eV \AA^{-1} . Then, the Monkhorst-Pack k-point sampling was set to $1 \times 3 \times 1$ [23]. The geometry optimizations were performed until the forces on each ion were reduced below 0.01 eV \AA^{-1} . The resulting structures were then used to calculate the electronic structures, and the k-point sampling was increased to $3 \times 5 \times 1$.

The Gibbs free-energy (ΔG_{H^*} or ΔG_{OH^*}) is calculated as:

$$\Delta G_{\text{H}^*} = \Delta E_{\text{H}^*} + \Delta E_{\text{ZPE}} - T \Delta S \quad (1)$$

$$\Delta G_{\text{OH}^*} = \Delta E_{\text{OH}^*} + \Delta E_{\text{ZPE}} - T \Delta S \quad (2)$$

The adsorption energy (ΔE_{H^*} or ΔE_{OH^*}) is calculated using the expression as follows.

$$\Delta E_{\text{H}^*} = E_{\text{H+surface}} - E_{\text{surface}} - E_{\text{H}} \quad (3)$$

$$\Delta E_{\text{OH}^*} = E_{\text{OH+surface}} - E_{\text{surface}} - E_{\text{H}} \quad (4)$$

where E_{surface} is the energy of the clean WO_2 (011) surface, E_{H} or E_{OH} represents the energy of the H atom or OH, and $E_{\text{H+surface}}$ or $E_{\text{OH+surface}}$ represents the total energy of the adsorbed system.

In summary, considering all the above factors, the following equations are obtained.

$$\Delta G_{\text{H}^*} = \Delta E_{\text{H}^*} + 0.24 \text{ eV} \quad (5)$$

$$\Delta G_{\text{OH}^*} = \Delta E_{\text{OH}^*} + 0.22 \text{ eV} \quad (6)$$

3. Results and discussion

3.1. Synthesis and Characterization

As displayed in Fig. 1a, the synthesis of $\text{Ni-WO}_x\text{@NF}$ is facile. In the beginning, the surface of pure NF is smooth, as shown in Fig. 1b. First, the NF was placed in dilute hydrochloric acid for a while to remove the oxide layer on its surface, and the surface of the pretreated NF (NF-pre) became rough (Fig. 1c). Therefore, the pretreatment of nickel foam can not only remove the oxide layer and promote the Ni in the NF to participate in the reaction but also provide a larger surface area for the attachment of the material. Then, through the hydrothermal reaction with a certain concentration of $(\text{NH}_4)_6\text{W}_7\text{O}_{24} \cdot 6\text{H}_2\text{O}$, a large number of nanorod-like precursors grow on the surface of the NF, as demonstrated in Fig. 1d. In this process, the NF not only acts as a carrier but also provides the source of nickel to participate in the hydrothermal process. Finally, $\text{Ni-WO}_x\text{@NF}$ is obtained by heat-treating the precursor material under N_2 and H_2 atmosphere, which still maintains the shape of nanorods, and the overall shape was like nano firecrackers, as demonstrated in Fig. 1e and Fig. S4a–b.

In the control experiments, when the concentration of $(\text{NH}_4)_6\text{W}_7\text{O}_{24} \cdot 6\text{H}_2\text{O}$ is low, the materials are nanosheet-like, as shown in Fig. S1a–b and Fig. S2a–b. The nanosheets of $\text{Ni-WO}_x\text{-5@NF}$ are sparse, and the nanosheets grown on the surface of the nickel foam are seen. However, the nanosheets of $\text{Ni-WO}_x\text{-10@NF}$ grow densely, and only the nanosheets grown vertically on the surface of nickel foam can be observed. However, when the concentration of $(\text{NH}_4)_6\text{W}_7\text{O}_{24} \cdot 6\text{H}_2\text{O}$ is higher, the materials are nanorod-like, as shown in Fig. S3a–b, Fig. S4a–b, and Fig. S5a–b. The nanorods of $\text{Ni-WO}_x\text{-20@NF}$ and $\text{Ni-WO}_x\text{-30@NF}$ grow regularly, most of them grow tightly and some grow staggered in the middle, resembling nano-firecrackers. At higher concentrations, the nanorods of $\text{Ni-WO}_x\text{-50@NF}$ self-assembled into nano-clusters. Therefore, nano-firecracker-like nickel-doped tungsten oxide can be synthesized at a certain concentration, with regular morphology and rough surface, which can expose more active sites for HER.

The lattice structure of the material was characterized by XRD. The XRD patterns of the synthesis process of $\text{Ni-WO}_x\text{@NF}$ are shown in Fig. S6a, in which $\text{Ni-WO}_x\text{@NF}$ -pre was heat-treated in an N_2 atmosphere to improve the crystallinity of the material. As shown in Fig. S6b, the diffraction peaks at 23.28° and 33.22° originate from monoclinic WO_3 (PDF#43-1035), while the peak at 44.16° is attributed to the cubic

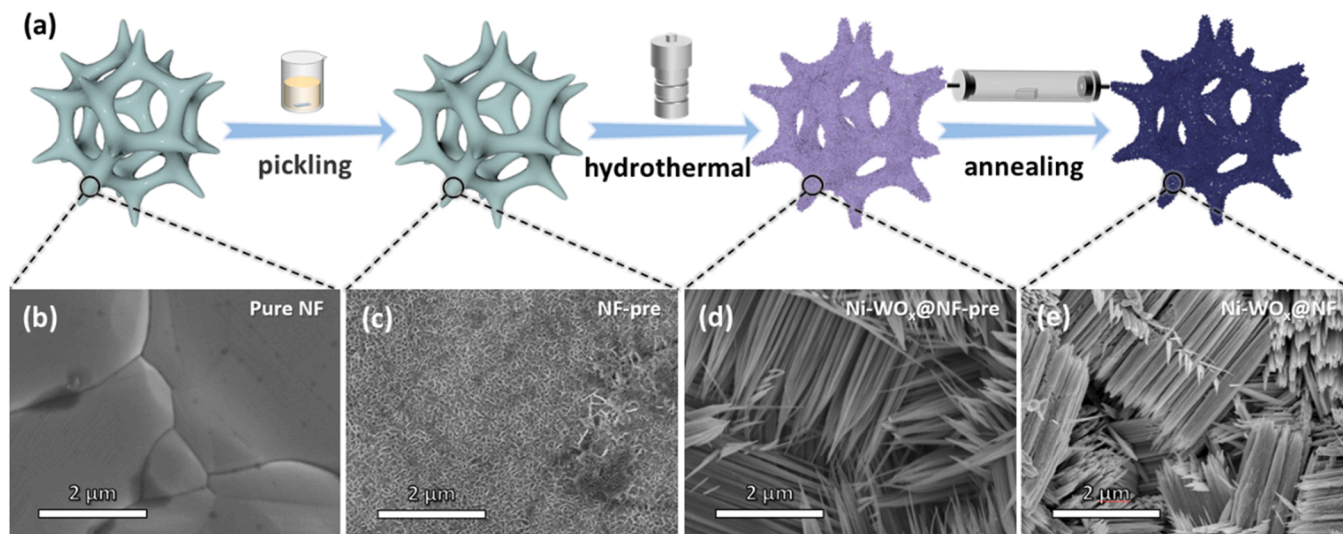


Fig. 1. (a) Schematic diagram of the synthesis of $\text{Ni-WO}_x\text{@NF}$. SEM images of (b) pure NF, (c) NF-pre, (d) $\text{Ni-WO}_x\text{@NF}$ -pre, and (e) $\text{Ni-WO}_x\text{@NF}$.

Ni (PDF#04-0850), indicating that the W in Ni-WO_x@NF-N₂ exists in the form of WO₃. After annealing in the H₂ atmosphere, the WO₃ on the surface of the material was reduced, and the XRD pattern of the Ni-WO_x@NF is shown in Fig. S7. The peaks of 25.54°, 36.70°, 52.72°, 59.74°, and 66.04° correspond to the crystal planes of (011), (−211), (220), (031), and (−231) of monocline WO₂ (PDF#32-1393), respectively. In addition, the diffraction peaks at 40.02° and 73.04° correspond to the (110) and (211) crystal planes of cubic phase W (PDF04-0806), while the peaks of 44.20°, 51.62°, and 76.06° correspond to the (111), (200) and (220) crystal planes of cubic Ni (PDF#04-0850). Furthermore, the XRD pattern of the Ni-WO_x exfoliated from NF was also analyzed, as shown in Fig. S8, in which no diffraction peaks of cubic Ni were found, indicating that the diffraction peaks of Ni of Ni-WO_x@NF were derived from the substrate NF. Moreover, in addition to the existence of WO₂ and W, there are diffraction peaks corresponding to WO₃ in the Ni-WO_x powder, indicating that part of WO₃ inside the material cannot be reduced to suboxide during annealing in H₂. To sum up, the interior of Ni-WO_x is a tungsten oxide material mixed with WO₃, WO₂, and W, while the surface of Ni-WO_x@NF is mainly composed of WO₂ and W.

Imitating the synthesis process of Ni-WO_x@NF, we tried to synthesize pure WO_x for comparison (Fig. S9 and Fig. S10a–d). Fig. 2a presents the XRD spectra of Ni-WO_x@NF and WO_x, and it can be seen that the XRD pattern of WO_x is roughly the same as Ni-WO_x@NF except for the diffraction peaks of cubic Ni provided by Ni.

The morphology and structure of the material were further characterized by transmission electron microscopy (TEM). As shown in Fig. 2b, the TEM results further prove that the material is in the shape of a nanorod, and the width of the illustrated nanorods is about 180 nm. The scanning transmission electron microscope energy dispersive X-ray (STEM-EDX) elemental map of Ni-WO_x is displayed in Fig. 2c–f. Ni, W, and O elements are evenly distributed in the nanorod, indicating that Ni is uniformly doped into the tungsten oxide. The lattice structure of Ni-WO_x was further illustrated using HRTEM, as exhibited in Fig. 2g–j. The interplanar fringes with the spacings of 0.3402 and 0.2291 nm correspond to the (011) plane of WO₂ and the (110) plane of W, respectively, indicating that WO_x is mainly composed of WO₂ and W, which is consistent with the XRD results. Furthermore, as shown in Fig. S11, the selected area electron diffraction (SAED) of Ni-WO_x clearly shows the

electron diffraction rings of the (110), (211), (310), (321), and (400) planes of metal W and the (033), (−321), (220), (121), (002), (020), and (011) planes of monoclinic WO₂, confirming that Ni-WO_x contains a mixture of W and WO₂. No Ni species was found in the SAED image, while the EDX images showed that the Ni element was uniformly distributed in the nanorod, which reconfirmed the previous conjecture that Ni was added to WO_x in the form of doping.

Raman spectroscopy is a very useful method to distinguish different phases of tungsten oxide. The Raman spectrum of Ni-WO_x@NF is shown in Fig. S12, in which typical fingerprint vibration modes at 127.6, 170.3, 187.7, 287.5, 333.2, 346.4, 481.8, 513.4, 600.3, 618.6, and 783.9 cm^{−1} are consistent with those of WO₂, indicating that the tungsten oxide on the surface of Ni-WO_x@NF mainly exists in the form of WO₂ [24]. The Raman spectrum of WO_x is consistent with that of Ni-WO_x@NF, as shown in Fig. 3a, indicating that the phase structure of tungsten oxide in WO_x is roughly the same as that of Ni-WO_x. As shown in Fig. S13, the peak at 135.2 cm^{−1} increases with the concentration of ammonium metatungstate, which corresponds to the characteristic peak of WO₃ [24]. This may be because higher concentrations can grow more WO₃ on the surface of the NF, which is not completely reduced during the H₂ annealing.

To understand the local electronic structure and geometry of Ni-WO_x, the X-ray Absorption Fine Structure (XAFS) based on synchrotron radiation was tested and analyzed, and its near-edge absorption fine structure is given in Fig. S14a, b. As shown in Fig. 3b, the k²-weighted Fourier transform of the extended X-ray absorption fine structure (EXAFS) revealed that the atomic distance (R) in Ni-WO_x is different from that of Ni, NiO, and Ni₂O₃. For Ni, the strong peak at 2.15 Å can be considered the peak of the Ni–Ni bond. For NiO, the peaks at 1.47 Å and 2.54 Å can be labeled as the peak of the Ni–O bond and Ni–Ni bond, respectively [25,26]. For the sample Ni-WO_x, the peaks at 1.56 Å and 2.66 Å correspond to the peaks of Ni–O and Ni–metal bonds, respectively. Therefore, the nickel in Ni-WO_x is neither nickel oxide nor metallic nickel. The k²-weight FT-EXAFS curves of W are shown in Fig. 3c, the R in Ni-WO_x is completely different from that of metal W, and the shape is similar to that of WO₂ and WO₃. Among them, the strong peak located at 1.47 Å corresponds to W=O bond or W–O bond [27,28].

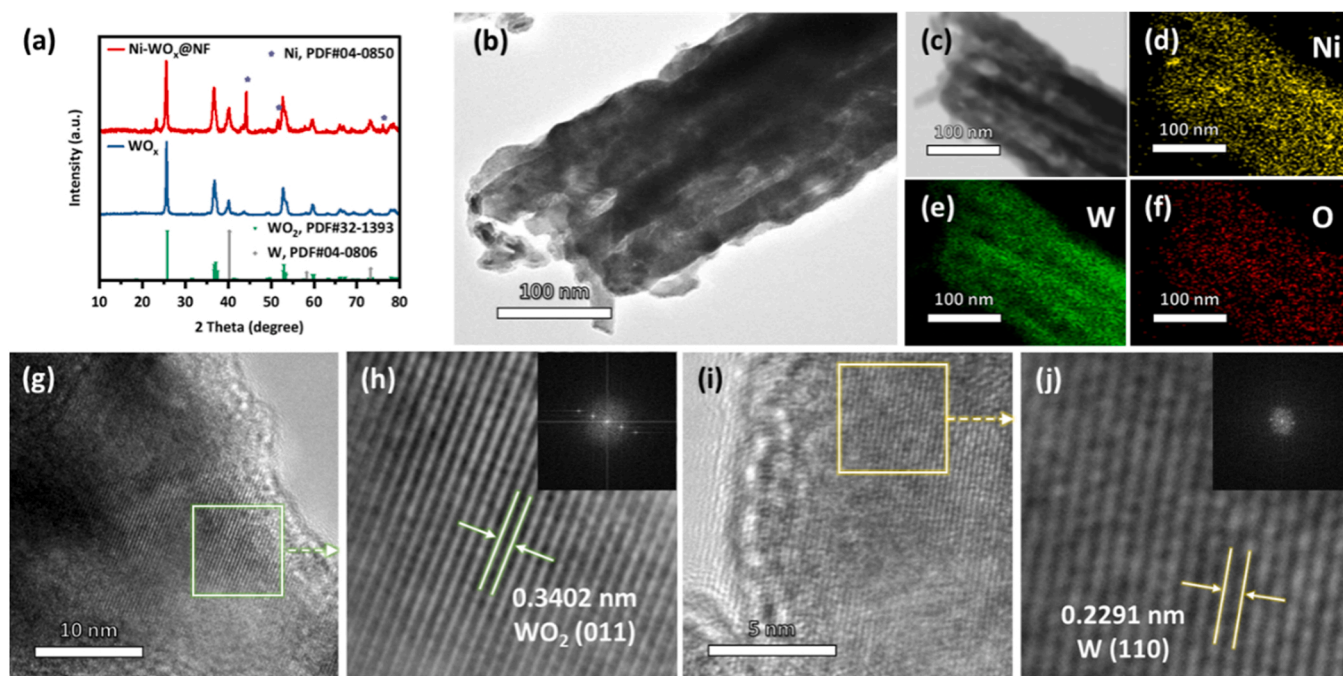


Fig. 2. (a) XRD patterns of Ni-WO_x@NF and WO_x. (b, c) TEM images of Ni-WO_x. (d–f) EDX images of Ni, W, and O elements. (g–j) HRTEM images of Ni-WO_x.

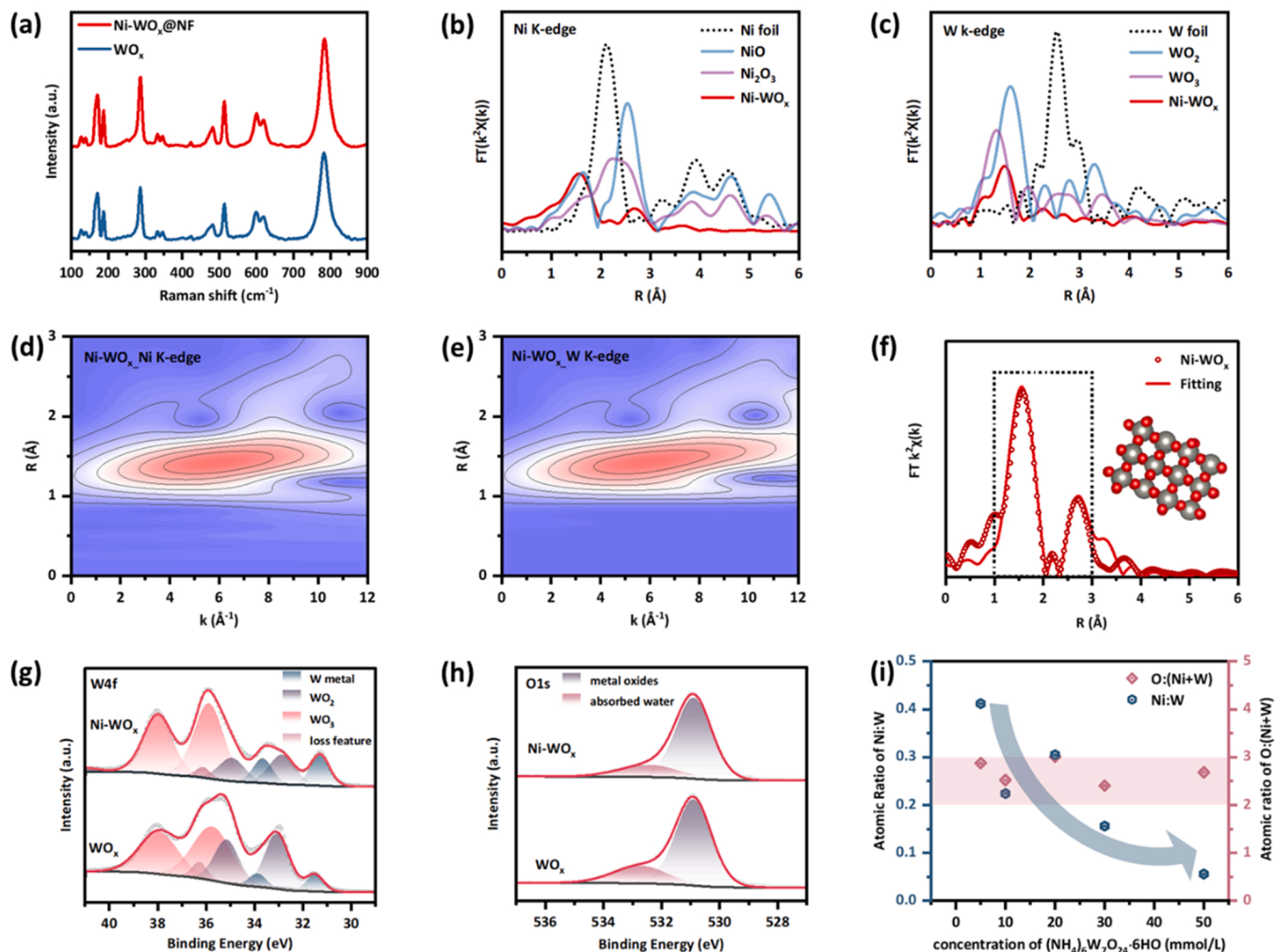


Fig. 3. (a) Raman spectrum of Ni-WO_x@NF and WO_x. (b) The k^2 -weight FT-EXAFS curves of Ni foil, NiO, Ni₂O₃, and Ni-WO_x at Ni K-edge. (c) The k^2 -weight FT-EXAFS curves of W foil, WO₂, WO₃, and Ni-WO_x at W L₃-edge. The k^2 -weight WT-EXAFS at (d) Ni K-edge and (e) W L₃-edge of Ni-WO_x. (f) Fitting the k^2 -weight FT-EXAFS curve of Ni-WO_x at Ni K-edge. XPS spectra of (g) W4f and (h) O1s of Ni-WO_x and WO_x. (i) The relationship of the atomic ratio of Ni: W and O: (Ni + W) to the concentration of (NH₄)₆W₇O₂₄·6H₂O in Ni-WO_x-m (m = 5, 10, 20, 30, 50).

The wavelet transform (WT) results in Fig. S15a, b and Fig. S16a, b show that the coordination characteristics of Ni in Ni-WO_x are different from those of NiO, while the coordination characteristics of W are matched with those of WO₂. As shown in Fig. 3d, e, the coordination properties of Ni of Ni-WO_x are similar to those of W, and the maximum intensity of R space is about 1.5 Å, corresponding to the Ni–O / W–O coordination [29]. Therefore, Ni in Ni-WO_x is doped into WO₂, replacing part of the W sites. To verify, the k^2 -weight FT-EXAFS curve of Ni-WO_x at the Ni K edge was fitted with WO₂ in the monoclinic phase [28]. The fitting curve is shown in Fig. 3f, and the relevant parameters are shown in Table S1. The WO₂ model well matches the k^2 -weight FT-EXAFS curve of Ni-WO_x at the Ni K edge, confirming that Ni is doped into WO_x to replace part of the W sites [12].

The composition of the samples was further characterized by XPS. As shown in Fig. S17, the spectra measured by XPS show that Ni-WO_x has signals from elements Ni, O, C and W, while WO_x also has signals from O, C, and W but no Ni signal. The high-resolution XPS spectrum of W4f is shown in Fig. 3g. The peaks at 31.29 and 33.66 eV belong to W4f_{7/2} and W4f_{5/2} of metal W, and the peaks at 32.86 and 34.93 eV of binding energy belong to the W4f_{7/2} and W4f_{5/2} peaks of WO₂, while the W4f_{7/2} and W4f_{5/2} peaks corresponding to WO₃ are located at the binding energies of 35.88 and 37.99 eV, respectively [30–33]. Furthermore, two small peaks located at 36.11 and 41.35 eV are the electron losses of metal W and WO₃, respectively [34,35]. Through peak area analysis, the

proportion of each phase in Ni-WO_x is obtained, as shown in Table S2, where the proportion of metal W and WO₂ is 18.1 % and 20.0 %, respectively. The high-resolution XPS spectrum of O1s is shown in Fig. 3h, where the peak at 532.44 eV is attributed to the Metal–O bond and the peak at 532.44 eV is attributed to the absorbed water [36–38]. The XPS spectrum of Ni2p is displayed in Fig. S18, and the three doublets at 856.32/873.97, 857.84/876.00, and 862.53/880.79 eV correspond to Ni²⁺, Ni³⁺, and satellite peaks, respectively [39].

Furthermore, the ratios of O: W and O: (Ni + W) for these samples are shown in Fig. 3i and Table S3. With the increase of the concentration of (NH₄)₆W₇O₂₄·6H₂O, the O: (Ni + W) distribution is in the range of 2–3, indicating that the valence state of W in the sample is between +2 and +3. Of particular interest, the Ni: W atomic ratio decreased with increasing the concentration of (NH₄)₆W₇O₂₄·6H₂O, indicating that the concentration of (NH₄)₆W₇O₂₄·6H₂O can affect the amount of Ni doping in Ni-WO_x. The Ni: W atomic ratio of Ni-WO_x-20 is higher than that of Ni-WO_x-10, which may be due to the different morphologies of the samples, and the nanorod-like material is easier to dope with Ni. Therefore, we obtained a series of nickel-doped tungsten oxide materials with different Ni doping amounts by adjusting the concentration of (NH₄)₆W₇O₂₄·6H₂O.

3.2. HER performance in alkaline media

The HER performance was tested in a three-electrode system, and the HER polarization curves are shown in Fig. 4a and Fig. S19. Pt/C@NF shows the best HER performance, with the overpotential of only 9.9 mV to achieve a current density of 10 mA cm^{-2} . Ni-WO_x@NF exhibits excellent HER activity in non-noble metal materials, achieving current densities of 10 and 100 mA cm^{-2} with overpotentials of 40.51 and 137.04 mV respectively. In contrast, WO_x@NF requires 170.92 mV to reach a current density of 10 mA cm^{-2} . The HER activity of Ni-WO_x@NF is much better than that of WO_x@NF, indicating that Ni doping can effectively enhance the HER kinetics, enabling efficient HER in alkaline media.

Tafel plots of these samples were acquired through the polarization curves of Fig. 4a, as shown in Fig. 4b. The Tafel slope of Ni-WO_x@NF is 40 mV dec^{-1} , which is significantly lower than that of WO_x@NF (101 mV dec^{-1}) and pure NF (91 mV dec^{-1}). The smaller Tafel slope indicates a faster HER process and better HER kinetics for the material. The electrochemical impedance spectra of the samples were analyzed and fitted, and the results are shown in Fig. 4c and Table S4. The charge transfer resistances (R_{ct}) of Ni-WO_x@NF and WO_x@NF are 1.192 and 18.39Ω , respectively. Ni-WO_x@NF has a smaller R_{ct} , indicating that Ni doping can accelerate the electron transfer of WO_x, and the HER process

is more likely to occur [40].

To explore the electrochemical intrinsic properties of these samples, a series of CV curves were collected in the small electrochemical window range of 50–150 mV, as shown in Fig. S20a–c. The electric double-layer capacitance (C_{dl}) was obtained by fitting and analyzing the difference of the current density and scanning speed of these samples, as shown in Fig. 4d. The C_{dl} values of Ni-WO_x@NF, WO_x@NF, and Pt/C@NF are 197.33, 60.26, and $260.23 \text{ mF cm}^{-2}$, respectively. The electrochemical active surface area (ECSA) is proportional to the C_{dl} , so the polarization curves in Fig. 4a were normalized to the C_{dl} to account for the intrinsic activity of these samples, as shown in Fig. S20d. The specific activities of Ni-WO_x@NF, WO_x@NF, and Pt/C@NF at 0.1 V were 0.27, 0.04, and 0.75 mA mF^{-1} , respectively. The specific activity of Ni-WO_x@NF is higher than that of WO_x@NF, indicating that Ni doping can promote the intrinsic activity of the HER of WO_x.

The HER polarization curves of the control experiments are presented in Fig. 4e, and the relationship between the amount of Ni doping and the overpotential of 10 mA cm^{-2} is shown in Fig. 4f. The amount of Ni doping decreases with the increase of the concentration of $(\text{NH}_4)_6\text{W}_7\text{O}_{24}\cdot 6\text{H}_2\text{O}$, and the overpotential of 10 mA cm^{-2} shows a volcanic relationship with the concentration of $(\text{NH}_4)_6\text{W}_7\text{O}_{24}\cdot 6\text{H}_2\text{O}$. Therefore, there is a volcanic relationship between the catalytic activity of Ni-WO_x and the amount of Ni doping. When the ratio of Ni to W is

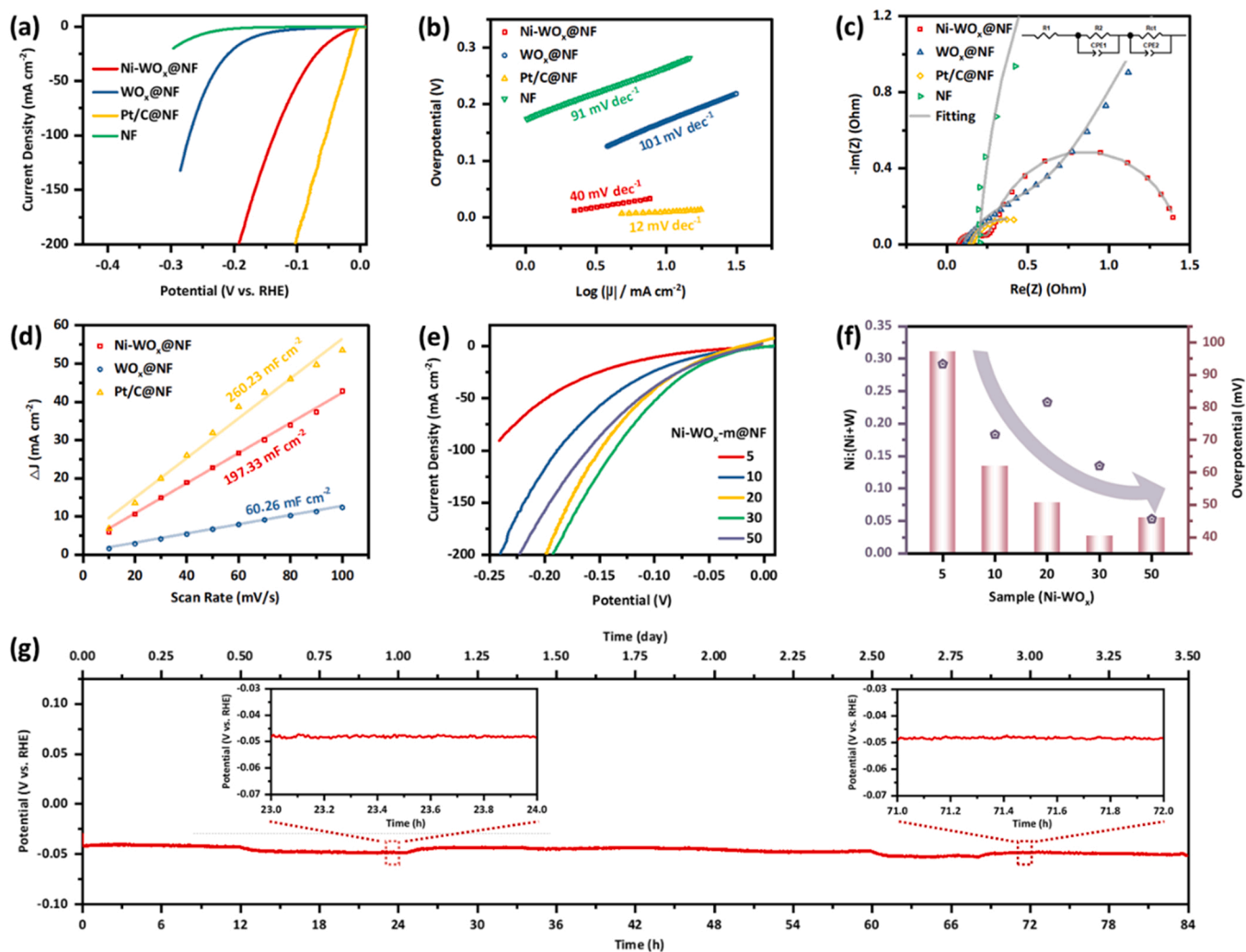


Fig. 4. (a) LSV curves, (b) Tafel slopes, and (c) Nyquist plots of Ni-WO_x@NF, WO_x@NF, Pt/C@NF, and pure NF towards the HER in 1 M KOH. (d) The relationship between charging current density differences (ΔJ) and the scan rate of Ni-WO_x@NF, WO_x@NF, and Pt/C@NF. (e) LSV curves and (f) the relationship of the amount of Ni doping and the overpotential at 10 mA cm^{-2} of Ni-WO_x-m@NF ($m = 5, 10, 20, 30, 50$) in 1 M KOH. (g) Potential-time curve of Ni-WO_x@NF at the current density of 10 mA cm^{-2} .

0.1563, Ni-WO_x@NF has the smallest overpotential and the best HER performance. The corresponding Nyquist plot and fitting results are shown in Fig. S21 and Table S5, Ni-WO_x@NF has the smallest Rct, indicating that a certain amount of Ni doping can accelerate electron transfer and enhance the HER activity of WO_x.

Moreover, the long-term stability of Ni-WO_x@NF at 10 mA cm⁻² was tested by chronopotentiometry (Fig. 4g), and the overpotential was almost unchanged after the stability test for 84 h. In addition, multi-current long-term stability tests and accelerated degradation tests (ADT) were also performed, as shown in Fig. S22 and Fig. S23. The XRD, SEM and XPS after the stability test are shown in Fig. S24, Fig. S25a, b, and Fig. S26a–d, which are consistent with the structure before the test, indicating that Ni-WO_x@NF has excellent HER stability. Therefore, Ni-WO_x@NF exhibits excellent stability, revealing its potential for commercial applications.

This strategy is also applicable to other transition metal doping. Cobalt-doped tungsten oxide (Co-WO_x@CF) was synthesized by a similar method, as shown in Fig. S27. As displayed in Fig. S28, Co-WO_x@CF achieve 10 mA cm⁻² with an overpotential of only 81.72 mV, which is much smaller than that of WO_x@CF (195.72 mV). Therefore, transition metal doping can improve the hydrogen evolution activity of

tungsten oxide, which can provide ideas for the design of non-precious metal HER electrocatalysts.

3.3. HER performance in alkaline seawater

Most HER catalysts are unstable during electrolysis in seawater, so it is a major challenge to explore efficient and stable HER electrocatalysts that can be used in seawater [41]. To investigate the HER performance in alkaline seawater, 1 M KOH sea salt solution and 1 M KOH seawater were configured as electrolytes.

In alkaline seawater, the HER polarization curves of the samples are shown in Fig. 5a and Fig. S29. The overpotentials required for Ni-WO_x@NF to reach 10 and 100 mA cm⁻² are 45.69 and 125.81 mV, respectively. Compared with WO_x@NF and pure NF, Ni-WO_x@NF exhibits the best HER performance. As exhibited in Fig. 5b, the Tafel slope of Ni-WO_x@NF is 46 mV dec⁻¹, which is close to the 14 mV dec⁻¹ of Pt/C@NF, and significantly smaller than that of WO_x@NF (114 mV dec⁻¹) and pure NF (87 mV dec⁻¹). Compared with WO_x@NF, the lower Tafel slope of Ni-WO_x@NF indicates that Ni doping well promotes the Volmer-Heyrovsky mechanism and accelerates HER dynamics [1,42].

The Nyquist plot and its fitting results are given in Fig. 5c and

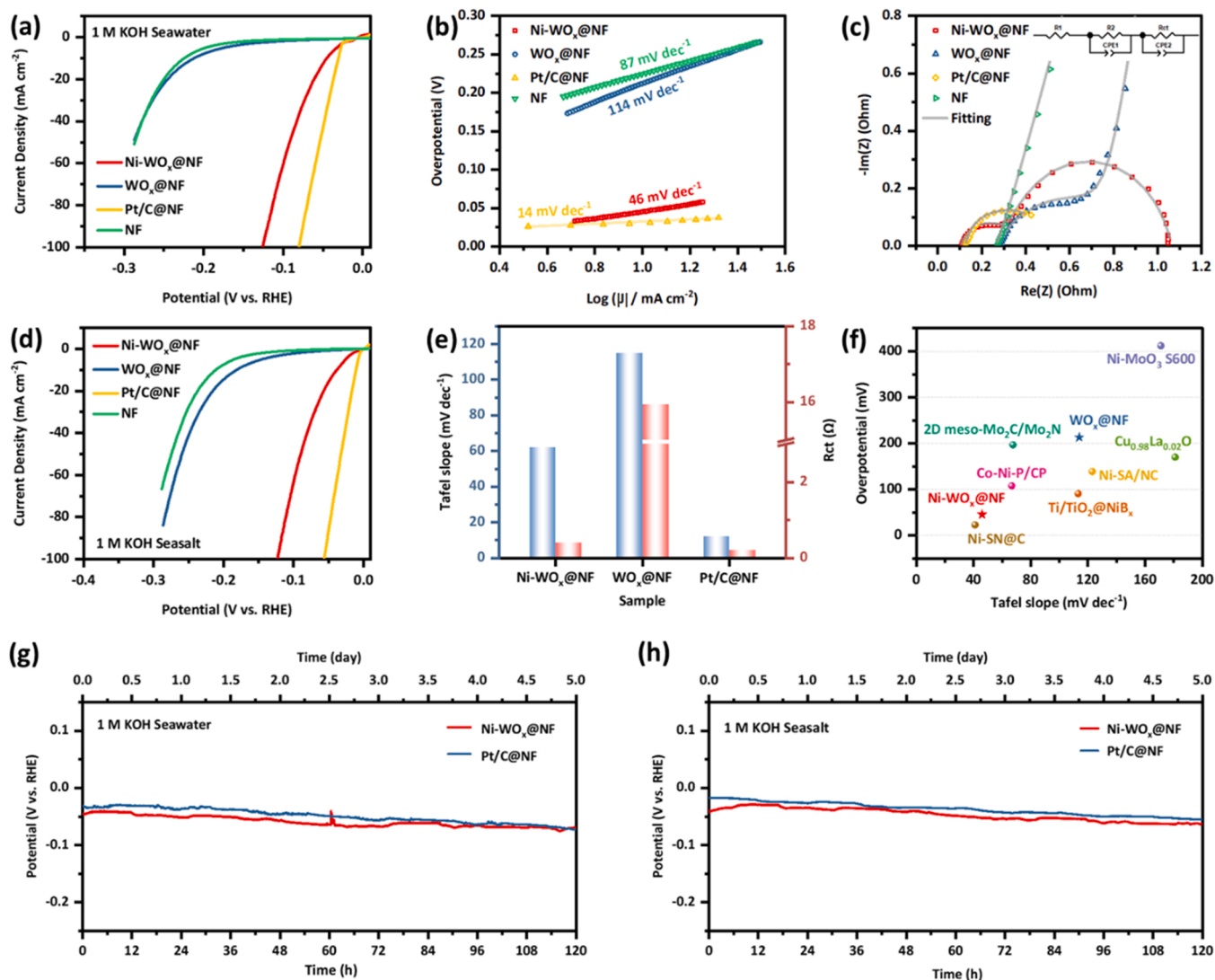


Fig. 5. (a) LSV curves, (b) Tafel slopes, and (c) Nyquist plots of Ni-WO_x@NF, WO_x@NF, Pt/C@NF, and pure NF towards the HER in 1 M KOH seawater. (d) LSV curves of these electrocatalysts towards the HER in 1 M KOH sea salt solution. (e) Tafel slopes and Rct of Ni-WO_x@NF, WO_x@NF, and Pt/C@NF in 1 M KOH sea salt solution. (f) Comparison of overpotential at 10 mA cm⁻² and Tafel slope of Ni-WO_x@NF, WO_x@NF, and recently reported HER electrocatalysts in alkaline seawater. Potential-time curves of Ni-WO_x@NF and Pt/C@NF during the HER in (g) 1 M KOH Seawater and (h) 1 M KOH Seasalt.

Table S6. Compared with 53.69 Ω of WO_x/NF , the Rct of $\text{Ni-WO}_x/\text{NF}$ is only 0.74332 Ω . The smaller charge transfer resistance indicates that nickel doping can effectively improve the charge transport ability of tungsten oxide in alkaline seawater.

To compare the intrinsic activity of the materials, the C_{dl} of $\text{Ni-WO}_x/\text{NF}$, WO_x/NF , and $\text{Pt/C}/\text{NF}$ were measured by the capacitance method to be 232.26, 56.03, and 114.91 mF cm^{-2} , respectively, as shown in Fig. S30a–d. $\text{Ni-WO}_x/\text{NF}$ has the largest C_{dl} , indicating that it has a better ECSA in alkaline seawater. The HER polarization curves of Fig. 5a normalized to the Cal are shown in Fig. S31. At -0.1 V, the specific activities of $\text{Ni-WO}_x/\text{NF}$, WO_x/NF , and $\text{Pt/C}/\text{NF}$ were 0.26, 0.03, and 1.22 mA mF^{-1} , respectively. And the specific activity of $\text{Ni-WO}_x/\text{NF}$ is significantly higher than that of WO_x/NF , suggesting that Ni doping helps to enhance the intrinsic HER activity in alkaline seawater.

Meanwhile, $\text{Ni-WO}_x/\text{NF}$ performs equally well in the hydrogen evolution reaction in 1 M KOH sea salt solution. $\text{Ni-WO}_x/\text{NF}$ exhibits excellent HER kinetics and a larger current response compared to WO_x/NF , requiring only an overpotential of 38.55 mV to reach a current density of 10 mA cm^{-2} (Fig. 5d and Fig. S32). As shown in Fig. 5e and Fig. S33a, the Tafel slope of $\text{Ni-WO}_x/\text{NF}$ is 62 mV dec^{-1} , which is lower than that of WO_x/NF , indicating that Ni doping can enhance the HER kinetics of tungsten oxide. As illustrated in Fig. 5e, Fig. S33b, and Table S7, the Rct of $\text{Ni-WO}_x/\text{NF}$ (0.39811 Ω) is much smaller than that of WO_x/NF and pure NF, showing that Ni doping can improve the

electronic conduction of WO_x in 1 M KOH sea salt solution and is more beneficial to the HER process. Furthermore, $\text{Ni-WO}_x/\text{NF}$ has a large ECSA, which helps to expose more active sites (Fig. S34a–d). And its specific activity is also better than that of WO_x/NF , which is 0.20 mA mF^{-1} at -0.1 V vs. RHE, as displayed in Fig. S35.

In general, nickel doping can effectively improve the hydrogen evolution activity of tungsten oxide in alkaline seawater. This strategy is also applicable for cobalt doping, as shown in Fig. S36 and Fig. S37. $\text{Co-WO}_x/\text{CF}$ achieved the HER current density of 10 mA cm^{-2} in alkaline seawater and alkaline sea salt solutions with an overpotential of 97.14 and 93.06 mV, respectively, significantly ahead of WO_x/CF . Therefore, transition metal doping is an effective strategy to improve the hydrogen evolution activity of tungsten oxide in alkaline seawater.

Crucially, the activity of $\text{Ni-WO}_x/\text{NF}$ was compared with other recently reported HER catalysts in alkaline seawater, as shown in Fig. 5f and Table S8. $\text{Ni-WO}_x/\text{NF}$ can achieve a current density of 10 mA cm^{-2} with only an overpotential of 45.69 mV in 1 M KOH seawater, with a low Tafel slope of 46 mV dec^{-1} , which is superior to the most recently reported HER electrocatalysts [17,43–48].

The long-term stability of $\text{Ni-WO}_x/\text{NF}$ and $\text{Pt/C}/\text{NF}$ in 1 M KOH seawater and 1 M KOH sea salt solution are shown in Fig. 5g and Fig. 5h. It is worth mentioning that in alkaline seawater, after a long-term test of 120 h, the overpotential of $\text{Ni-WO}_x/\text{NF}$ decreased by only 24.32 mV, while that of $\text{Pt/C}/\text{NF}$ decreased by 41.29 mV. Furthermore, $\text{Ni-WO}_x/\text{NF}$ showed lower HER activity than $\text{Pt/C}/\text{NF}$ at the beginning,

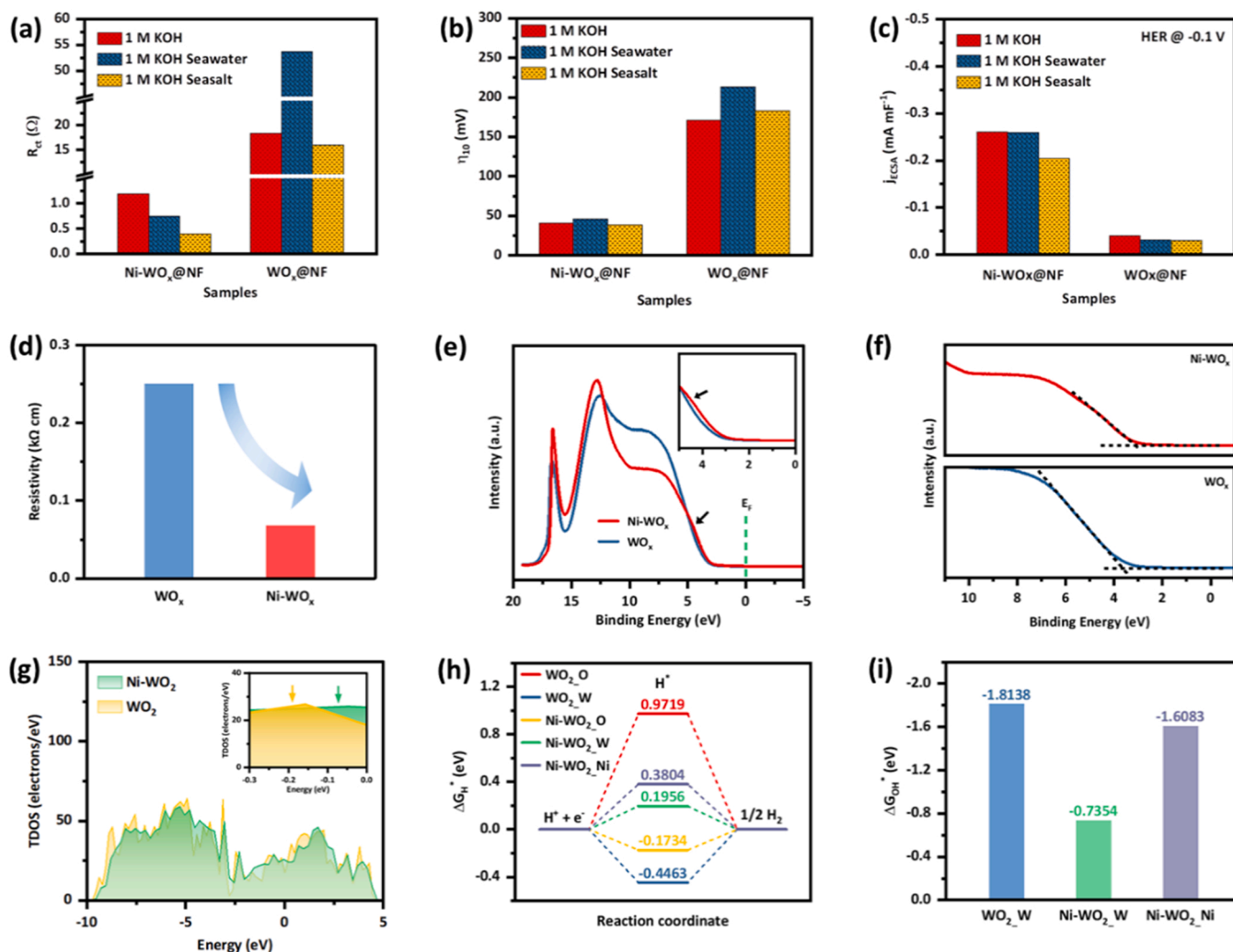


Fig. 6. (a) Rct, (b) η_{10} , and (c) j_{ECSA} of $\text{Ni-WO}_x/\text{NF}$ and WO_x/NF . (d) Resistivity and (e–f) UPS spectra for Ni-WO_x and WO_x . (g) The calculated total density of states for Ni-WO_2 and WO_2 . The calculated adsorption free energy of (h) H^* and (i) OH^* on different sites in Ni-WO_2 and pure WO_2 .

but after 120 h of stability test, it exhibited higher HER activity than Pt/C/NF. Thus, the excellent stability in alkaline seawater indicates that Ni-WO_x/NF has great potential for commercialization.

3.4. Analysis of HER activity

Experimentally, it is proved that nickel doping can reduce the charge transfer resistance of tungsten oxide and improve the HER activity in alkaline freshwater and alkaline seawater environments (Fig. 6a–c). The resistivity of Ni-WO_x and WO_x was measured by the four-point probe method, and the results are shown in Fig. 6d and Table S9. In general, nickel doping can effectively reduce the resistivity of tungsten oxide, and the conductivity of Ni-WO_x is 0.068 kΩ cm, which is significantly superior to that of WO_x of 0.25 kΩ cm [49].

Fig. 6e compares the UPS spectra of Ni-WO_x and WO_x. A slight hump around the Fermi level (~4.5 eV) was observed in Ni-WO_x, indicating that Ni doping can effectively increase the electron density around the Fermi level of WO_x, which may regulate the adsorption free energy of WO_x, thereby improving HER/HOR kinetics. [50,51] In addition, the secondary electron tail threshold of Ni-WO_x is shifted by 0.58 eV in the direction of lower kinetic energy compared with that of WO_x (Fig. 6f), indicating that the work function is reduced by 0.58 eV [52]. Catalysts with lower work functions are more favorable for electrocatalytic reactions. Therefore, the lower work function of Ni-WO_x indicates an easier ability to transfer electrons, thus improving electrocatalysis [53].

To further explain the mechanism of Ni doping improving HER performance of tungsten oxide, DFT calculations were performed using the model shown in Fig. S38a, b. The density of states (DOS) is an important indicator of HER performance, and excellent HER electrocatalysts usually have high DOS near the Fermi level [1]. For both WO₂ and Ni-WO₂, the density of electron states near the Fermi level is mainly contributed by d electrons of W, while the density of electron states below the Fermi level is mainly contributed by p electrons of O (Fig. S39a–f and Fig. S40a–h). And the total DOS of both WO₂ and Ni-WO₂ near the Fermi level is not 0, showing conductor properties. Moreover, Ni doping increases the contribution of d electrons of W, p electrons of O and d electrons of Ni near the Fermi level, so the electron density of Ni-WO₂ near the Fermi level is higher than that of WO₂, as illustrated in Fig. 6g. Ni-WO₂ has a higher electron density of states near the Fermi level, indicating that nickel doping can enhance the conductivity of tungsten oxide, which is consistent with the result of R_{ct} in Fig. 6a [54].

The hydrogen adsorption free energy (ΔG_H^*) and hydroxide adsorption free energy (ΔG_{OH}^*) are considered as descriptors of HER, so the ΔG_H^* and ΔG_{OH}^* of Ni-WO₂ and WO₂ are evaluated. The models for calculating ΔG_H^* at various sites on the two models are shown in Fig. S41a, b, and Fig. S42a–c, and the results are presented in Fig. 6e. In general, the hydrogen adsorption free energy of the O site of Ni-WO₂ is -0.1734 eV, which is closest to the optimal value of 0 eV for an ideal HER electrocatalyst [55,56].

Furthermore, the calculation models of hydroxide adsorption on the W sites of WO₂ and Ni-WO₂ are shown in Fig. S43a, b. After Ni doping, the ΔG_{OH}^* at the W site increases from -1.8138 to -0.7354 eV, as displayed in Fig. 6f. The weakened OH adsorption is closer to the optimum value of the hydroxide adsorption free energy of -0.30 eV [57]. In summary, Ni doping optimizes the ΔG_H^* at the O site and the ΔG_{OH}^* at the W site of WO₂, thereby enhancing the HER activity of tungsten oxide.

4. Conclusion

In this work, nickel-doped tungsten oxide is proposed to exhibit excellent HER performance in alkaline seawater. It was confirmed by XRD, XPS, TEM, and XAS that Ni in Ni-WO_x was added to WO_x by doping, replacing part of the W sites. Theoretical calculations show that nickel doping can enhance the density of states of tungsten oxide at the Fermi level and optimize the H adsorption at the O site and the OH

adsorption at the W site. The prepared Ni-WO_x/NF exhibits excellent HER activity, requiring only 137.04 and 125.81 mV to achieve HER current density of 100 mA cm⁻² in 1 M KOH and alkaline seawater, respectively. Therefore, this work verifies the effect of nickel doping on the HER activity of tungsten oxide and provides a new strategy for the design of efficient electrocatalysts for alkaline seawater.

CRediT authorship contribution statement

Wanli Liang: Investigation, Data curation, Conceptualization, Validation, Writing – original draft. **Mengyan Zhou:** Data curation, Validation. **Xinyi Lin:** Data curation, Validation, Investigation. **Jinchang Xu:** Data curation. **Pengyu Dong:** Investigation. **Zhichen Le:** Validation. **Muzi Yang:** Investigation. **Jian Chen:** Investigation. **Fangyan Xie:** Investigation. **Nan Wang:** Supervision. **Yanshuo Jin:** Conceptualization, Writing – review & editing, Supervision, Funding acquisition. **Hui Meng:** Funding acquisition, Supervision. All authors have agreed to the signature to the author list.

Declaration of Competing Interest

The authors declare that they have no known competing financial interests or personal relationships that could have appeared to influence the work reported in this paper.

Data Availability

No data was used for the research described in the article.

Acknowledgments

This work was supported by the National Natural Science Foundation of China (22075102, 22005120), and the Science and Technology Planning Project of Guangzhou, China (202102020310).

Appendix A. Supporting information

Supplementary data associated with this article can be found in the online version at doi:10.1016/j.apcatb.2023.122397.

References

- [1] P.K.L. Tran, D.T. Tran, D. Malhotra, S. Prabhakaran, D.H. Kim, N.H. Kim, J.H. Lee, Highly effective freshwater and seawater electrolysis enabled by atomic Rh-modulated Co-CoO lateral heterostructures, *Small* 17 (2021) 2103826, <https://doi.org/10.1002/sml.202103826>.
- [2] S. Wang, P. Yang, X. Sun, H. Xing, J. Hu, P. Chen, Z. Cui, W. Zhu, Z. Ma, Synthesis of 3D heterostructure Co-doped Fe₂P electrocatalyst for overall seawater electrolysis, *Appl. Catal. B Environ.* 297 (2021), 120386, <https://doi.org/10.1016/j.apcatb.2021.120386>.
- [3] W. Xu, G. Fan, S. Zhu, Y. Liang, Z. Cui, Z. Li, H. Jiang, S. Wu, F. Cheng, Electronic structure modulation of nanoporous cobalt phosphide by carbon doping for alkaline hydrogen evolution reaction, *Adv. Funct. Mater.* 31 (2021) 2107333, <https://doi.org/10.1002/adfm.202107333>.
- [4] H. Chen, Y. Zou, J. Li, K. Zhang, Y. Xia, B. Hui, D. Yang, Wood aerogel-derived sandwich-like layered nanoelectrodes for alkaline overall seawater electrosplitting, *Appl. Catal. B Environ.* 293 (2021), 120215, <https://doi.org/10.1016/j.apcatb.2021.120215>.
- [5] B. Zhang, W. Xu, S. Liu, X. Chen, T. Ma, G. Wang, Z. Lu, J. Sun, Enhanced interface interaction in Cu₂S@Ni core-shell nanorod arrays as hydrogen evolution reaction electrode for alkaline seawater electrolysis, *J. Power Sources* 506 (2021), 230235, <https://doi.org/10.1016/j.jpowsour.2021.230235>.
- [6] J. Zheng, Binary platinum alloy electrodes for hydrogen and oxygen evolutions by seawater splitting, *Appl. Surf. Sci.* 413 (2017) 72–82, <https://doi.org/10.1016/j.apsusc.2017.04.016>.
- [7] T. Zheng, W. Sang, Z. He, Q. Wei, B. Chen, H. Li, C. Cao, R. Huang, X. Yan, B. Pan, S. Zhou, J. Zeng, Conductive tungsten oxide nanosheets for highly efficient hydrogen evolution, *Nano Lett.* 17 (2017) 7968–7973, <https://doi.org/10.1021/acs.nanolett.7b04430>.
- [8] D. Wang, H. Li, N. Du, W. Hou, Single platinum atoms immobilized on monolayer tungsten trioxide nanosheets as an efficient electrocatalyst for hydrogen evolution reaction, *Adv. Funct. Mater.* 31 (2021) 2009770, <https://doi.org/10.1002/adfm.202009770>.

- [9] T.H. Wondimu, A.W. Bayeh, D.M. Kabtamu, Q. Xu, P. Leung, A.A. Shah, Recent progress on tungsten oxide-based materials for the hydrogen and oxygen evolution reactions, *Int. J. Hydrog. Energy* 47 (2022) 20378–20397, <https://doi.org/10.1016/j.ijhydene.2022.04.226>.
- [10] Y. Zhao, S. Wei, L. Xia, K. Pan, B. Zhang, H. Huang, Z. Dong, H.-H. Wu, J. Lin, H. Pang, Sintered Ni metal as a matrix of robust self-supporting electrode for ultra-stable hydrogen evolution, *Chem. Eng. J.* 430 (2022), 133040, <https://doi.org/10.1016/j.cej.2021.133040>.
- [11] X. Yu, Z.-Y. Yu, X.-L. Zhang, Y.-R. Zheng, Y. Duan, Q. Gao, R. Wu, B. Sun, M.-R. Gao, G. Wang, S.-H. Yu, “Superaerophobic” nickel phosphide nanorod catalyst for efficient hydrogen evolution at ultrahigh current densities, *J. Am. Chem. Soc.* 141 (2019) 7537–7543, <https://doi.org/10.1021/jacs.9b02527>.
- [12] Z. Dan, W. Liang, X. Gong, X. Lin, W. Zhang, Z. Le, F. Xie, J. Chen, M. Yang, N. Wang, Y. Jin, H. Meng, Substitutional doping engineering toward W2N nanorod for hydrogen evolution reaction at high current density, *ACS Mater. Lett.* 4 (2022) 1374–1380, <https://doi.org/10.1021/acsmaterlett.2c00324>.
- [13] L. Yu, L. Wu, B. McElhenny, S. Song, D. Luo, F. Zhang, Y. Yu, S. Chen, Z. Ren, Ultrafast room-temperature synthesis of porous S-doped Ni/Fe (oxy)hydroxide electrodes for oxygen evolution catalysis in seawater splitting, *Energy Environ. Sci.* 13 (2020) 3439–3446, <https://doi.org/10.1039/D0EE00921K>.
- [14] H. Zhou, F. Yu, Y. Huang, J. Sun, Z. Zhu, R.J. Nielsen, R. He, J. Bao, W. A. Goddard III, S. Chen, Z. Ren, Efficient hydrogen evolution by ternary molybdenum sulfoselenide particles on self-standing porous nickel diselenide foam, *Nat. Commun.* 7 (2016) 12765, <https://doi.org/10.1038/ncomms12765>.
- [15] Y. Jin, H. Wang, J. Li, X. Yue, Y. Han, P.K. Shen, Y. Cui, Porous MoO₂ nanosheets as non-noble bifunctional electrocatalysts for overall water splitting, *Adv. Mater.* 28 (2016) 3785–3790, <https://doi.org/10.1002/adma.201506314>.
- [16] B. Ravel, M. Newville, ATHENA, ARTEMIS, HEPHAESTUS: data analysis for X-ray absorption spectroscopy using IFEFFIT, *J. Synchrotron Radiat.* 12 (2005) 537–541, <https://doi.org/10.1107/S0909049050102719>.
- [17] H. Jin, X. Wang, C. Tang, A. Vasileff, L. Li, A. Slattery, S. Qiao, Stable and highly efficient hydrogen evolution from seawater enabled by an unsaturated nickel surface nitride, *Adv. Mater.* 33 (2021) 2007508, <https://doi.org/10.1002/adma.202007508>.
- [18] G. Kresse, J. Hafner, Ab initio molecular-dynamics simulation of the liquid-metalamorphous-semiconductor transition in germanium, *Phys. Rev. B* 49 (1994) 14251–14269, <https://doi.org/10.1103/PhysRevB.49.14251>.
- [19] G. Kresse, J. Furthmüller, Efficient iterative schemes for ab initio total-energy calculations using a plane-wave basis set, *Phys. Rev. B* 54 (1996) 11169–11186, <https://doi.org/10.1103/PhysRevB.54.11169>.
- [20] P.E. Blöchl, Projector augmented-wave method, *Phys. Rev. B* 50 (1994) 17953–17979, <https://doi.org/10.1103/PhysRevB.50.17953>.
- [21] G. Kresse, D. Joubert, From ultrasoft pseudopotentials to the projector augmented-wave method, *Phys. Rev. B* 59 (1999) 1758–1775, <https://doi.org/10.1103/PhysRevB.59.1758>.
- [22] B. Hammer, L.B. Hansen, J.K. Nørskov, Improved adsorption energetics within density-functional theory using revised Perdew-Burke-Ernzerhof functionals, *Phys. Rev. B* 59 (1999) 7413–7421, <https://doi.org/10.1103/PhysRevB.59.7413>.
- [23] H.J. Monkhorst, J.D. Pack, Special points for Brillouin-zone integrations, *Phys. Rev. B* 13 (1976) 5188–5192, <https://doi.org/10.1103/PhysRevB.13.5188>.
- [24] F. Liu, L. Li, F. Mo, J. Chen, S. Deng, N. Xu, A catalyzed-growth route to directly form micropatterned WO₂ and WO₃ nanowire arrays with excellent field emission behaviors at low temperature, *Cryst. Growth Des.* 10 (2010) 5193–5199, <https://doi.org/10.1021/cg100995f>.
- [25] H. Zeng, S. Chen, Y.Q. Jin, J. Li, J. Song, Z. Le, G. Liang, H. Zhang, F. Xie, J. Chen, Y. Jin, X. Chen, H. Meng, Electron density modulation of metallic MoO₂ by Ni doping to produce excellent hydrogen evolution and oxidation activities in acid, *ACS Energy Lett.* 5 (2020) 1908–1915, <https://doi.org/10.1021/acscenergylett.0c00642>.
- [26] Y. Luo, Z. Zhang, F. Yang, J. Li, Z. Liu, W. Ren, S. Zhang, B. Liu, Stabilized hydroxide-mediated nickel-based electrocatalysts for high-current-density hydrogen evolution in alkaline media, *Energy Environ. Sci.* 14 (2021) 4610–4619, <https://doi.org/10.1039/D1EE01487K>.
- [27] J.G. Howell, Y. Li, A.T. Bell, Propene metathesis over supported tungsten oxide catalysts: a study of active site formation, *ACS Catal.* 6 (2016) 7728–7738, <https://doi.org/10.1021/acscatal.6b01842>.
- [28] W. Chen, J. Pei, C.-T. He, J. Wan, H. Ren, Y. Wang, J. Dong, K. Wu, W.-C. Cheong, J. Mao, X. Zheng, W. Yan, Z. Zhuang, C. Chen, Q. Peng, D. Wang, Y. Li, Single tungsten atoms supported on MOF-derived N-doped carbon for robust electrochemical hydrogen evolution, *Adv. Mater.* 30 (2018) 1800396, <https://doi.org/10.1002/adma.201800396>.
- [29] J. Song, Y.Q. Jin, L. Zhang, P. Dong, J. Li, F. Xie, H. Zhang, J. Chen, Y. Jin, H. Meng, X. Sun, Phase-separated Mo–Ni alloy for hydrogen oxidation and evolution reactions with high activity and enhanced stability, *Adv. Energy Mater.* 11 (2021) 2003511, <https://doi.org/10.1002/aenm.202003511>.
- [30] V. Marascu, A. Lazea-Stoyanova, A. Bonciu, V. Satulu, G. Dinescu, Tungsten particles fabrication by a microjet discharge, *Mater. Res. Express* 7 (2020), 066509, <https://doi.org/10.1088/2053-1591/ab955d>.
- [31] Q. Guan, G. Yun, W. Li, Tuning hydrodearomatization performance of interstitial Ni₁₀ alloy catalyst by controlling the doping of a small amount of tungsten, *Catal. Today* 364 (2021) 202–210, <https://doi.org/10.1016/j.cattod.2020.04.011>.
- [32] T.H. Wondimu, G.-C. Chen, H.-Y. Chen, D.M. Kabtamu, A.W. Bayeh, K.-C. Wang, H.-C. Huang, C.-H. Wang, High catalytic activity of oxygen-vacancy-rich tungsten oxide nanowires supported by nitrogen-doped reduced graphene oxide for the hydrogen evolution reaction, *J. Mater. Chem. A* 6 (2018) 19767–19774, <https://doi.org/10.1039/C8TA07000H>.
- [33] M. Saleem, M.F. Al-Kuhaili, S.M.A. Durrani, A.H.Y. Hendi, I.A. Bakhtiari, S. Ali, Influence of hydrogen annealing on the optoelectronic properties of WO₃ thin films, *Int. J. Hydrog. Energy* 40 (2015) 12343–12351, <https://doi.org/10.1016/j.ijhydene.2015.06.078>.
- [34] X.F. Lu, L. Yu, J. Zhang, X.W. (David) Lou, Ultrafine dual-phased carbide nanocrystals confined in porous nitrogen-doped carbon dodecahedrons for efficient hydrogen evolution reaction, *Adv. Mater.* 31 (2019) 1900699, <https://doi.org/10.1002/adma.201900699>.
- [35] Z. Chen, R. Zheng, M. Graš, W. Wei, G. Lota, H. Chen, B.-J. Ni, Tuning electronic property and surface reconstruction of amorphous iron borides via W-P co-doping for highly efficient oxygen evolution, *Appl. Catal. B Environ.* 288 (2021), 120037, <https://doi.org/10.1016/j.apcatb.2021.120037>.
- [36] X. Li, H. Zhang, Y. Liu, X. Duan, X. Xu, S. Liu, H. Sun, S. Wang, Synergy of NiO quantum dots and temperature on enhanced photocatalytic and thermophoto hydrogen evolution, *Chem. Eng. J.* 390 (2020), 124634, <https://doi.org/10.1016/j.cej.2020.124634>.
- [37] T. Tang, W.-J. Jiang, S. Niu, N. Liu, H. Luo, Q. Zhang, W. Wen, Y.-Y. Chen, L.-B. Huang, F. Gao, J.-S. Hu, Kinetically controlled coprecipitation for general fast synthesis of sandwiched metal hydroxide nanosheets/graphene composites toward efficient water splitting, *Adv. Funct. Mater.* 28 (2018) 1704594, <https://doi.org/10.1002/adfm.201704594>.
- [38] H. Wang, Y. Wang, J. Zhang, X. Liu, S. Tao, Electronic structure engineering through Fe-doping CoP enables hydrogen evolution coupled with electro-Fenton, *Nano Energy* 84 (2021), 105943, <https://doi.org/10.1016/j.nanoen.2021.105943>.
- [39] X. Shi, X. Ling, L. Li, C. Zhong, Y. Deng, X. Han, W. Hu, Nanosheets assembled into nickel sulfide nanospheres with enriched Ni³⁺ active sites for efficient water-splitting and zinc-air batteries, *J. Mater. Chem. A* 7 (2019) 23787–23793, <https://doi.org/10.1039/C9TA03819a>.
- [40] K.L. Zhou, C. Wang, Z. Wang, C.B. Han, Q. Zhang, X. Ke, J. Liu, H. Wang, Seamlessly conductive Co(OH)₂ tailored atomically dispersed Pt electrocatalyst with a hierarchical nanostructure for an efficient hydrogen evolution reaction, *Energy Environ. Sci.* 13 (2020) 3082–3092, <https://doi.org/10.1039/D0EE01347A>.
- [41] Y.-Y. Ma, C.-X. Wu, X.-J. Feng, H.-Q. Tan, L.-K. Yan, Y. Liu, Z.-H. Kang, E.-B. Wang, Y.-G. Li, Highly efficient hydrogen evolution from seawater by a low-cost and stable CoMoP/C electrocatalyst superior to Pt/C, *Energy Environ. Sci.* 10 (2017) 788–798, <https://doi.org/10.1039/C6EE03768B>.
- [42] S. Shin, Z. Jin, D.H. Kwon, R. Bose, Y. Min, High turnover frequency of hydrogen evolution reaction on amorphous MoS₂ thin film directly grown by atomic layer deposition, *Langmuir* 31 (2015) 1196–1202, <https://doi.org/10.1021/la504162u>.
- [43] S. Li, Z. Zhao, T. Ma, P. Pachfule, A. Thomas, Superstructures of organic–polyoxometalate co-crystals as precursors for hydrogen evolution electrocatalysts, *Angew. Chem. Int. Ed.* 61 (2022), <https://doi.org/10.1002/anie.202112298>.
- [44] C. Fu, S. Weng, J. Fan, Y. Zhang, Y. Guo, W. Hao, Boron-based materials modified on the surface of TiO₂ nanorods via electrodeless plating toward high-efficient solar-driven water splitting, *Chem. Eng. J.* 430 (2022), 132881, <https://doi.org/10.1016/j.cej.2021.132881>.
- [45] T. Yang, Y. Xu, H. Lv, M. Wang, X. Cui, G. Liu, L. Jiang, Triggering the intrinsic catalytic activity of Ni-doped molybdenum oxides via phase engineering for hydrogen evolution and application in Mg/seawater batteries, *ACS Sustain. Chem. Eng.* 9 (2021) 13106–13113, <https://doi.org/10.1021/acscuschemeng.1c05184>.
- [46] Z. Yu, J. Xu, L. Meng, L. Liu, Efficient hydrogen production by saline water electrolysis at high current densities without the interfering chlorine evolution, *J. Mater. Chem. A* 9 (2021) 22248–22253, <https://doi.org/10.1039/D1TA05703K>.
- [47] J.D. Rodney, S. Deepapriya, M.C. Robinson, S.J. Das, S. Perumal, P. Sivakumar, H. Jung, B.C. Kim, C.J. Raj, Cu_{1-x}RE_xO (RE = La, Dy) decorated dendritic Ni nanorods for highly efficient splitting of seawater into hydrogen and oxygen fuels, *Appl. Mater. Today* 24 (2021), 101079, <https://doi.org/10.1016/j.apmt.2021.101079>.
- [48] W. Zang, T. Sun, T. Yang, S. Xi, M. Waqar, Z. Kou, Z. Lyu, Y.P. Feng, J. Wang, S. J. Pennycook, Efficient hydrogen evolution of oxidized Ni-N₃ defective sites for alkaline freshwater and seawater electrolysis, *Adv. Mater.* 33 (2021) 2003846, <https://doi.org/10.1002/adma.202003846>.
- [49] D.H. Youn, S. Han, J.Y. Kim, J.Y. Kim, H. Park, S.H. Choi, J.S. Lee, Highly active and stable hydrogen evolution electrocatalysts based on molybdenum compounds on carbon nanotube–graphene hybrid support, *ACS Nano* 8 (2014) 5164–5173, <https://doi.org/10.1021/nn5012144>.
- [50] Y. Zhan, F. Xie, H. Zhang, Z. Lin, J. Huang, W. Zhang, X. Sun, H. Meng, Y. Zhang, J. Chen, Metallic Ni promoted Mo₂C–MoN particles supported on N-doped graphitic carbon as bifunctional catalyst for oxygen and hydrogen evolution reaction in alkaline media, *J. Electrochem. Soc.* 165 (2018) F75–F81, <https://doi.org/10.1149/2.0891802jes>.
- [51] Z. Shi, K. Nie, Z.-J. Shao, B. Gao, H. Lin, H. Zhang, B. Liu, Y. Wang, Y. Zhang, X. Sun, X.-M. Cao, P. Hu, Q. Gao, Y. Tang, Phosphorus–Mo₂C@carbon nanowires toward efficient electrochemical hydrogen evolution: composition, structural and electronic regulation, *Energy Environ. Sci.* 10 (2017) 1262–1271, <https://doi.org/10.1039/C7EE00388A>.
- [52] Y. Zhan, H. Zeng, F. Xie, H. Zhang, W. Zhang, Y. Jin, Y. Zhang, J. Chen, H. Meng, Templated growth of Fe/N/C catalyst on hierarchically porous carbon for oxygen reduction reaction in proton exchange membrane fuel cells, *J. Power Sources* 431 (2019) 31–39, <https://doi.org/10.1016/j.jpowsour.2019.05.051>.
- [53] F.-Y. Gao, S.-N. Liu, J.-C. Ge, X.-L. Zhang, L. Zhu, Y.-R. Zheng, Y. Duan, S. Qin, W. Dong, X. Yu, R.-C. Bao, P.-P. Yang, Z.-Z. Niu, Z.-G. Ding, W. Liu, S. Lan, M.-R. Gao, Y. Yan, S.-H. Yu, Nickel–molybdenum–niobium metallic glass for efficient

- hydrogen oxidation in hydroxide exchange membrane fuel cells, *Nat. Catal.* (2022), <https://doi.org/10.1038/s41929-022-00862-8>.
- [54] Y. Jiang, P. Sun, L. Sharma, B. Mao, R. Kakkar, T. Meng, L. Zheng, M. Cao, Further insights into bifunctional mechanism in alkaline hydrogen evolution for hybridized nanocatalysts and general route toward mechanism-oriented synthesis, *Nano Energy* 81 (2021), 105645, <https://doi.org/10.1016/j.nanoen.2020.105645>.
- [55] J.K. Nørskov, T. Bligaard, A. Logadottir, J.R. Kitchin, J.G. Chen, S. Pandalov, U. Stimming, Trends in the exchange current for hydrogen evolution, *J. Electrochem. Soc.* 152 (2005) J23–J26, <https://doi.org/10.1149/1.1856988>.
- [56] J. Lu, S. Yin, P.K. Shen, Carbon-encapsulated electrocatalysts for the hydrogen evolution reaction, *Electrochem. Energy Rev.* 2 (2019) 105–127, <https://doi.org/10.1007/s41918-018-0025-9>.
- [57] I.T. McCrum, M.T.M. Koper, The role of adsorbed hydroxide in hydrogen evolution reaction kinetics on modified platinum, *Nat. Energy* 5 (2020) 891–899, <https://doi.org/10.1038/s41560-020-00710-8>.